5048 *Biochemistry* **2010,** *49,* 5048–5056
DOI: 10.1021/bi1005046

BIOCHEMISTRY
including biophysical chemistry & molecular biology
Article

Structures of Metal-Substituted Human Histone Deacetylase 8 Provide Mechanistic Inferences on Biological Function[†,‡]

Daniel P. Dowling,[§] Samuel G. Gattis,[∥] Carol A. Fierke,[∥] and David W. Christianson*[,§]

[§]*Roy and Diana Vagelos Laboratories, Department of Chemistry, University of Pennsylvania, Philadelphia, Pennsylvania 19104-6323, and* [∥]*Departments of Chemistry and Biological Chemistry, University of Michigan, 930 North University Avenue, Ann Arbor, Michigan 48109-1055*

Received April 2, 2010; Revised Manuscript Received May 13, 2010

ABSTRACT: The metal-dependent histone deacetylases (HDACs) adopt an α/β protein fold first identified in rat liver arginase. Despite insignificant overall amino acid sequence identity, these enzymes share a strictly conserved metal binding site with divergent metal specificity and stoichiometry. HDAC8, originally thought to be a Zn^{2+}-metallohydrolase, exhibits increased activity with Co^{2+} and Fe^{2+} cofactors based on k_{cat}/K_M (Gantt, S. L., Gattis, S. G., and Fierke, C. A. (2006) *Biochemistry 45*, 6170−6178). Here, we report the first X-ray crystal structures of metallo-substituted HDAC8, Co^{2+}-HDAC8, D101L Co^{2+}-HDAC8, D101L Mn^{2+}-HDAC8, and D101L Fe^{2+}-HDAC8, each complexed with the inhibitor M344. Metal content of protein samples in solution is confirmed by inductively coupled plasma mass spectrometry. For the crystalline enzymes, peaks in Bijvoet difference Fourier maps calculated from X-ray diffraction data collected near the respective elemental absorption edges confirm metal substitution. Additional solution studies confirm incorporation of Cu^{2+}; Fe^{3+} and Ni^{2+} do not bind under conditions tested. The metal dependence of the substrate K_M values and the K_i values of hydroxamate inhibitors that chelate the active site metal are consistent with substrate−metal coordination in the precatalytic Michaelis complex that enhances catalysis. Additionally, although HDAC8 binds Zn^{2+} nearly 10^6-fold more tightly than Fe^{2+}, the affinities for both metal ions are comparable to the readily exchangeable metal concentrations estimated in living cells, suggesting that HDAC8 could bind either or both Fe^{2+} or Zn^{2+} *in vivo*.

Posttranslational acetylation of the lysine side chain is documented in many proteins and has diverse effects on protein activity (*1*). For example, acetylation of lysine residues at the N-termini of histone proteins in the nucleosome is critical for regulating the accessibility of the genetic code during replication, transcription, and repair (*2*−*6*). Among the array of covalent modifications described to date in defining the "histone code", those involving histone lysine residues are particularly intriguing. Acetylation and deacetylation reactions are catalyzed by the enzymes histone acetyltransferase and histone deacetylase (HDAC),[1] respectively. The acetylation of histone lysine residues alters interactions with the DNA backbone, e.g., as observed in the X-ray crystal structure of the nucleosome (*7*). Additionally, proteins containing the bromo domain have increased binding affinity for other proteins containing acetyl-L-lysine residues, implicating acetylation in the regulation of protein−protein interactions (*8*−*12*).

There are 18 known HDAC enzymes divided phylogenetically into four classes: class I (HDAC1−3 and HDAC8), class II (HDAC4−7 and HDAC9,10), class III (sirtuins 1−7), and class IV (HDAC11) (*13*). Class I, II, and IV HDACs are metalloenzymes that require a divalent metal ion for substrate binding and catalysis. The class III enzymes, termed sirtuins due to their homology with yeast Sir2, have a protein fold and catalytic mechanism that differ from those of class I, II, and IV enzymes. Although the class I, II, and IV enzymes are referred to as histone deacetylases based on genomic sequence mining using the first identified HDAC (HDAC1; see ref *14*), HDAC enzymes can function to deacetylate many acetylated protein substrates in addition to histones and in various cellular locations beyond the nucleus (*15*). For example, while the class I enzyme HDAC8 is localized within the nucleus (*14*, *16*), HDAC8 is also found in the cytosol of smooth muscle cells where it associates with the α-actin cytoskeleton (*17*, *18*). In another example, class II HDAC enzymes are shuttled back and forth between the nucleus and cytosol depending on their interaction with the 14-3-3 transporter protein, which is mediated by phosphorylation (*19*).

Class I, II, and IV HDAC enzymes adopt the α/β fold first observed for the binuclear manganese metalloenzyme arginase, despite sharing extremely low amino acid sequence identity (less than 13%) (*20*, *21*). Arginase catalyzes the hydrolysis of L-arginine to form L-ornithine and urea. The first structure of a histone deacetylase-like protein from *Aquifex aeolicus* revealed a conserved metal binding site in the active site, corresponding to the

[†]This work was supported by National Institutes of Health Grants GM49758 (D.W.C.) and GM40602 (C.A.F.).

[‡]The atomic coordinates of the wild-type Co^{2+}-HDAC8-M344 complex, the D101L Co^{2+}-HDAC8-M344 complex, the D101L Fe^{2+}-HDAC8-M344 complex, and the D101L Mn^{2+}-HDAC8-M344 complex have been deposited in the Protein Data Bank (www.rcsb.org) with accession codes 3MZ3, 3MZ7, 3MZ6, and 3MZ4, respectively.

*To whom correspondence should be addressed: Tel: 215-898-5714. Fax: 215-573-2201. E-mail: chris@sas.upenn.edu.

[1]Abbreviations: APAH, acetylpolyamine amidohydrolase; EDTA, ethylenediaminetetraacetic acid; HDAC, histone deacetylase; HDLP, histone deacetylase-like protein; ICP, inductively coupled plasma; M344, 4-(dimethylamino)-*N*-[7-(hydroxyamino)-7-oxoheptyl]benzamide; MES, 2-(*N*-morpholino)ethanesulfonic acid; MOPS, 3-(*N*-morpholino)-propanesulfonic acid; NTA, nitrilotriacetic acid; TCEP, tris(2-carboxyethyl)phosphine; SOD, superoxide dismutase.

 Published on Web 05/27/2010

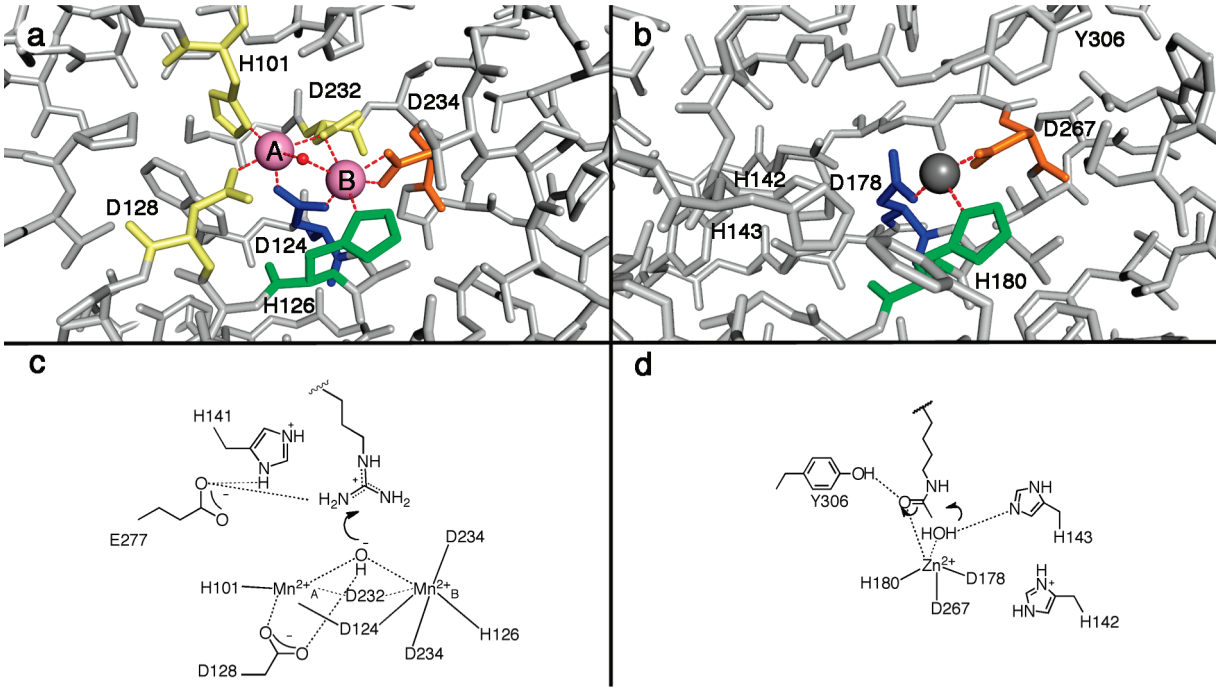

FIGURE 1: (a) Binuclear manganese cluster in rat arginase I (1RLA) (*20*); Mn^{2+} ions appear as pink spheres, and the metal-bridging hydroxide ion is shown as a red sphere. (b) Zinc binding site in HDAC8 (1T64) (*23*); the Zn^{2+} ion appears as a gray sphere, and the zinc-bound inhibitor trichostatin A is not shown for clarity. Metal ligands topologically identical to those in rat arginase I are color-coded accordingly. (c) First step in the proposed arginase mechanism (*67*, *68*). (d) First step in the proposed HDAC8 mechanism (*21*, *36*, *47*).

Mn_B^{2+} site of arginase, in which a single catalytic Zn^{2+} ion is coordinated by two aspartate residues and a histidine residue (Figure 1) (*21*). Subsequently determined crystal structures of human HDAC8, HDAC4, HDAC7, and bacterial histone deacetylase-like amidohydrolase reveal strict conservation of this metal binding site (*22*−*26*). In contrast, the Mn_A^{2+} site of arginase is not conserved in HDAC enzymes.

While it is clear that a single transition metal ion is required for catalysis by HDAC enzymes, the precise identity of the physiologically relevant metal ion is somewhat ambiguous. Intriguingly, the active site metal ligands of HDAC and HDAC-like enzymes (Asp_2His) are unusual for a zinc-dependent hydrolase (Figure 1). Considering the presence of two negatively charged aspartate residues, which are considered "hard" ligands, the binding of a "hard" metal ion is expected, e.g., the Mn^{2+} ions found in the active site of arginase (*20*). Moreover, activity measurements reveal that the catalytic efficiency (k_{cat}/K_M) of HDAC8 is enhanced in the presence of Co^{2+} and Fe^{2+} compared with Zn^{2+} (*27*). Notably, many metallohydrolases are activated by a single Fe^{2+} ion for catalysis, including peptide deformylase, methionyl aminopeptidase, LuxS, γ-carbonic anhydrase, cytosine deaminase, atrazine chlorohydrolase, and UDP-3-*O*-((*R*)-3-hydroxymyristoyl)-*N*-acetylglucosamine deacetylase (LpxC) (*28*−*35*). Some of these metalloenzymes were initially mischaracterized as Zn^{2+}-metallohydrolases due to the facile oxidation of Fe^{2+} to Fe^{3+}, which then dissociated and thereby allowed the binding of adventitious Zn^{2+} (*28*, *30*). It is possible that HDAC enzymes have been similarly mischaracterized.

Here, we report the X-ray crystal structures of HDAC8 containing the high-activity metal ions Co^{2+} or Fe^{2+} as well as the low-activity metal ion Mn^{2+} with a bound hydroxamate inhibitor. Metal ion content is confirmed in solution by inductively coupled plasma mass spectrometry and in the crystal by Bijvoet difference Fourier analysis. These results, along with affinity data of HDAC8 for the physiologically relevant metal ions Zn^{2+} and Fe^{2+}, highlight the evolution of metal ion selectivity and stoichiometry in arginase and arginase-related metalloenzymes such as HDAC.

MATERIALS AND METHODS

Protein Preparation. Recombinant HDAC8-His was prepared and purified as previously described (*36*) and concentrated to 2−12 mg/mL for metal exchange dialysis. To prevent trace metal contamination, all plasticware was presoaked with 1 mM ethylenediaminetetraacetic acid (EDTA) and triple rinsed with Millipure H_2O; glassware was not used in these experiments. Plastic disposables, including pipet tips and microcentrifuge tubes, were certified trace metal-free. Sodium hydroxide (Sigma, 99.999%) was used to titrate 3-(*N*-morpholino)propanesulfonic acid (MOPS) buffer (Ambion). Dialysis cassettes (Pierce) and syringes with needles were presoaked with 1 mM EDTA and extensively washed with Millipure H_2O. When necessary, anaerobic conditions were achieved using either the *captair pyramid* glovebag filled with argon or nitrogen or an anaerobic chamber (Coy, Grass Lake, MI).

Metal-free HDAC8 was generated by dialyzing purified HDAC8 twice into 500 mL of 25 mM MOPS (pH 7.0), 1 mM EDTA, and 10 μM dipicolinic acid, followed by buffer exchange into 25 mM MOPS (pH 7.5) and 0.1 mM EDTA and finally 25 mM MOPS (pH 7.5) and 1 μM EDTA. Crystallization buffer (50 mM Tris (pH 8.0), 150 mM KCl, 5% glycerol, and 1 mM tris(2-carboxyethyl)phosphine (TCEP; added to maintain reduced cysteines and/or Fe^{2+})) was pretreated with Chelex resin (Sigma) and used for the final dialysis. To prepare each metal-substituted enzyme, the metal-free enzyme was dialyzed into crystallization buffer supplemented with 100 μM either $CoCl_2$, $FeCl_2$, $MnCl_2$, $CuCl_2$ (Sigma, 99.999%), $NiCl_2$, or $FeCl_3$ (Hampton Research, > 98%), followed by a final dialysis into crystallization

Table 1: Data Collection and Refinement Statistics

structure	wild-type Co^{2+}-HDAC8-M334 complex	D101L Co^{2+}-HDAC8-M334 complex	D101L Fe^{2+}-HDAC8-M334 complex	D101L Mn^{2+}-HDAC8-M334 complex
resolution limits (Å)	50−3.2	50−1.9	50−2.0	50−1.85
energy/wavelength (eV/Å)	7725/1.6050	11566/1.0720	11566/1.0720	12660/0.9793
space group	$P2_1$	$P2_12_12$	$P2_12_12$	$P2_12_12_1$
total/unique reflections	28240/14687	63065/33586	53795/28881	137178/72518
completeness (%) (overall/outer shell)	98.3/90.9	97.5/85.4	98.7/90.5	99.0/98.0
R_{merge}[a] (overall/outer shell)	0.132/0.441	0.049/0.492	0.064/0.254	0.099/0.406
$I/\sigma(I)$ (overall/outer shell)	9.9/2.3	38/2.4	28.1/5.2	19.2/4.1
no. of reflections (work set/test set)	12996/684	28790/1576	25924/1457	54828/6936
R/R_{free}[b]	0.204/0.256	0.220/0.256	0.202/0.247	0.201/0.249
rms deviations				
bond lengths (Å)	0.008	0.014	0.015	0.012
bond angles (deg)	1.3	1.4	1.4	1.2

[a] $R_{merge} = \sum|I - \langle I\rangle|/\sum|I|$, where I is the observed intensity and $\langle I\rangle$ is the average intensity calculated for replicate data. [b] Crystallographic R factor, $R = \sum||F_o| - |F_c||/\sum|F_o|$, for reflections contained in the working set. Free R factor, $R_{free} = \sum||F_o| - |F_c||/\sum|F_o|$, for reflections contained in the test set excluded from refinement. $|F_o|$ and $|F_c|$are the observed and calculated structure factor amplitudes, respectively.

buffer pretreated with Chelex resin to remove any excess unbound divalent metal ions. Metal content was quantified by inductively coupled plasma emission mass spectrometry (ICP-MS) using a facility in the Geology Department at the University of Michigan. Protein concentrations were determined by Bradford analysis (*37*) to determine metal:protein ratios.

Inhibitor Affinity Measurements. The concentration of metal-free HDAC8 was determined using Ellman's reagent, as previously described (*27*). Apo-HDAC8 was incubated with equimolar $CoCl_2$, $FeCl_2$, or $ZnCl_2$ on ice for 1 h, and metallo-substituted HDAC8 (0.5 μM) was assayed with 50 μM Fluor de Lys HDAC8 substrate (BIOMOL) at 25 °C in 25 mM Tris (pH 8.0), 140 mM NaCl, and 2.7 mM KCl pretreated with Chelex resin. Fe^{2+}-HDAC8 activity was measured in the presence of 5 mM sodium dithionite; these conditions have no effect on enzyme activity when tested with Zn^{2+}-HDAC8. Assays were stopped with Developer II solution (BIOMOL) and 10 μM trichostatin A. Inhibition constants (K_i) were calculated for a minimum of 12 inhibitor concentrations using the Cheng−Prusoff equation (*38*).

Protein Crystallization. Considering that HDAC8 does not readily crystallize without a bound ligand, complexes with the inhibitor 4-(dimethylamino)-*N*-[7-(hydroxyamino)-7-oxoheptyl]-benzamide (designated "M344" (*23*, *39*)) were prepared to obtain diffraction quality crystals. The inhibitor M344 was purchased from Sigma and used without further purification for cocrystallization experiments (2 mM). Since D101L HDAC8 generally yielded better quality crystals that diffracted to higher resolution, both wild-type and mutant enzymes were used for crystallographic studies. For crystallization of Co^{2+}- or Mn^{2+}-substituted enzymes, a 4 μL sitting drop of 5 mg/mL Co^{2+}- or Mn^{2+}-HDAC8-M344 complex was mixed with a 4 μL drop of precipitant buffer (0.1 M 2-(*N*-morpholino)ethanesulfonic acid (MES) (pH 5.3), 0−5% polyethylene glycol (PEG) monomethyl ether (MME) 550, 2 mM TCEP, and 0.03 mM Gly-Gly-Gly, pretreated with Chelex resin) and equilibrated against a 600 μL reservoir of precipitant buffer at room temperature. Crystals formed after 3−4 weeks for the D101L and wild-type Co^{2+}-HDAC8-M344 complexes and 1−2 days for the D101L and wild-type Mn^{2+}-HDAC8-M344 complexes. Suitable crystals of the Co^{2+}-HDAC8-M344 complexes were harvested and cryoprotected in 25 mM Tris-HCl, 50 mM MES (pH 5.8), 75 mM KCl, 0.5 mM TCEP, 50 μM M344, 10% PEG MME 550, and 30% glycerol and flash cooled in liquid nitrogen. The wild-type Mn^{2+}-HDAC8-M344 complex yielded thin clusters of plate-like crystals; however, the D101L Mn^{2+}-HDAC8-M344 complex formed higher quality crystals that were harvested and cryoprotected in 30% Jeffamine ED-2001 and 0.1 M HEPES (pH 7.0) and flash cooled in liquid nitrogen.

For crystallization of the Fe^{2+}-substituted enzyme, a 4 μL sitting drop of 5 mg/mL Fe^{2+}-HDAC8-M344 complex was mixed with a 4 μL drop of precipitant buffer (0.1 M MES (pH 6.8), 10−18% PEG 35K, 2 mM TCEP, and 0.03 M Gly-Gly-Gly, pretreated with Chelex resin) and equilibrated against a 600 μL reservoir of precipitant buffer at room temperature. Sodium dithionite was added to the reservoir before sealing with crystallization tape, and trays were stored under a nitrogen atmosphere using either the *captair pyramid* glovebag or a desiccator equipped with a vacuum and gas port. Wild-type Fe^{2+}-HDAC8 complexed with M344 formed plate-like crystals within 1−2 days that were unsuitable for X-ray data collection. However, crystals of the D101L Fe^{2+}-HDAC8-M344 complex were larger and more suitable for X-ray data collection. Crystals were harvested and cryoprotected in 25 mM Tris-HCl, 50 mM MES (pH 6.8), 75 mM KCl, 0.5 mM TCEP, 50 μM M344, 20% PEG 2000, and 20% glycerol under a nitrogen atmosphere and flash cooled in liquid nitrogen.

Data Collection and Structure Determination. Diffraction data for Co^{2+}- and Fe^{2+}-HDAC8 samples were measured on beamline 24-ID-C at the Advanced Photon Source, Northeastern Collaborative Access Team (APS, NECAT, Argonne, IL). Data for the D101L Co^{2+}- and Fe^{2+}-HDAC8-M344 structures were collected at 11.566 keV/1.0720 Å; for the measurement of Bijvoet differences, data were collected at 7.725 keV/1.6050 Å or 7.120 keV/1.7143 Å for Co^{2+} or Fe^{2+} derivatives, respectively. Data for the D101L Mn^{2+}-HDAC8-M344 structure were collected on our home source (Rigaku IV++ image plate area detector mounted on a Rigaku RU200HB rotating anode X-ray generator; 8.048 keV/1.5406 Å) and on beamline X25 at the National Synchrotron Light Source (NSLS, Brookhaven National Laboratory, New York). Crystallographic and data collection statistics are recorded in Tables 1 and 2. Data were indexed and merged using HKL2000 (*40*). Molecular replacement calculations were performed with PHASER (*41*) using the

Table 2: Anomalous Scattering Data Collection Statistics

structure	D101L Co^{2+}-HDAC8-M334 complex	D101L Fe^{2+}-HDAC8-M334 complex	D101L Mn^{2+}-HDAC8-M334 complex
resolution limits (Å)	50−2.7	50−3.0	35−2.7
energy/wavelength (eV/Å)	7725/1.6050	7120/1.7143	8048/1.5406
space group	$P2_12_12$	$P2_12_12$	$P2_12_12_1$
total/unique reflections	21310/11556	19561/10633	42388/22990
completeness (%) (overall/outer shell)	99.9/100.0	98.5/89.1	95.7/97.8
redundancy (overall/outer shell)	8.4/8.3	8.2/4.8	6.5/6.4
R_{merge}[a] (overall/outer shell)	0.162/0.567	0.129/0.230	0.126/0.461
$I/\sigma(I)$ (overall/outer shell)	13.0/5.2	15.7/4.8	11.2/4.4

[a] $R_{merge} = \sum|I - \langle I\rangle|/\sum|I|$, where I is the observed intensity and $\langle I\rangle$ is the average intensity calculated for replicate data.

Table 3: Metal Ion Content of Metallo-Substituted HDAC8

	molar ratio of metal:protein[a,b]					
	Fe	Co	Ni	Cu	Zn	Mn
native HDAC8[c]	0.06	−[d]	−	0.13	0.87	ND[e]
Co^{2+}-HDAC8	0.02	1.1	−	0.01	0.02	ND
Fe^{2+}-HDAC8	0.79	0.08	−	0.08	0.05	ND
Fe^{2+}-D101L HDAC8	1.4	−	−	0.07	0.05	ND
Fe^{3+}-HDAC8	0.12	−	−	0.02	0.05	−
Fe^{3+}-D101L HDAC8	−	−	−	0.06	0.08	−
Mn^{2+}-HDAC8	0.02	−	0.02	0.06	0.25	1.1
Mn^{2+}-D101L HDAC8	−	0.05	−	0.04	0.06	0.98
Cu^{2+}-HDAC8	0.01	−	−	1.09	0.14	ND
Ni^{2+}-HDAC8	ND	0.02	0.14	0.08	0.13	−

[a] Metallo-substituted HDAC8 was generated as described in Materials and Methods. Metal-free enzyme was generated by dialyzing with EDTA. Each metal ion was subsequently introduced at a concentration of 100 μM chloride salt and dialyzed to a final concentration of 100 nM. Metal ion content of final protein samples was determined by ICP mass spectrometry. [b] The ratio of metal ion to protein was determined by dividing the metal ion concentration, as determined by ICP mass spectrometry, by the protein concentration, as determined by Bradford assay. [c] Native HDAC8 refers to recombinant protein expressed in *E. coli* with 100 μM $ZnCl_2$. [d] (−) signifies a value of less than 0.01. [e] ND signifies not determined.

structure of either wild-type or D101L HDAC8 (PDB accession codes 1W22 or 3EW8, respectively) minus ligands and solvent atoms as a search probe. Iterative cycles of refinement were performed using CNS (*42*) or REFMAC (*43*) for wild-type or D101L HDAC8, respectively, and models were fit into electron density maps using COOT (*44*). Bijvoet difference Fourier maps were generated using CNS (*42*). At the conclusion of refinement, residues M1−S13 at the N-terminus and 7−9 residues between E85−E95 appeared to be disordered in all monomers and were excluded from each final model. Data collection and refinement statistics are recorded in Table 1.

Metal Affinity Measurements. The affinity of HDAC8 for Zn^{2+} and Fe^{2+} was measured from an increase in activity in the presence of increasing concentrations of free Zn^{2+} or Fe^{2+} maintained using a metal buffer in an anaerobic glovebox. The standard assay buffer was replaced with 1 mM nitrilotriacetic acid (NTA), 147 mM NaCl, 2.7 mM KCl, 5 mM MOPS (pH 7) (*45*, *46*) with $[Fe^{2+}]_{total}$ = 0−950 μM ($[Fe^{2+}]_{free}$ 0−2.6 μM) or $[Zn^{2+}]_{total}$ = 0−200 μM ($[Zn^{2+}]_{free}$ 0−532 pM), and 0.4 μM HDAC8. The concentration of bound versus free metal ion was calculated using the program MINEQL+ (Environmental Research Software). The assay mixtures, containing all components except substrate, were incubated for 4 h on ice in the anaerobic glovebox. Assays were incubated at 30 °C for 30 min, initiated by the addition of substrate (50 μM final), and the products were analyzed as described above. The activity is dependent on the concentration of $[Me^{2+}]_{free}$ and not the total concentration of the metal ion and buffer. The metal dissociation constant (K_{Me}) was determined from fitting a binding isotherm (eq 1) to the activity versus $[Me^{2+}]_{free}$ data using the program KaleidaGraph (Synergy Software) where A is the activity at saturating metal ion.

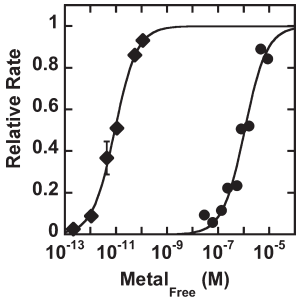

FIGURE 2: Metal affinity of HDAC8. The activity of HDAC8 was assayed in the presence of increasing concentrations of free Zn^{2+} (diamonds) or Fe^{2+} (circles) using a metal buffer, as described in Materials and Methods. The relative initial velocity (v_{obs}/v_{max}) is plotted to simplify the graph. Under these conditions the activity of Fe^{2+}-HDAC8 is 2.8-fold higher than that of Zn^{2+}-HDAC8 (*27*). The metal dissociation constant was determined from fitting a single binding isotherm (eq 1) to these data.

$$v = \frac{A}{1 + \frac{K_{Me}}{[Me^{2+}]_{free}}} \quad (1)$$

RESULTS

Metal Affinity Studies. Essentially complete metal ion substitution of HDAC8 with Co^{2+}, Fe^{2+}, Mn^{2+}, or Cu^{2+} is confirmed by the ICP mass spectrometry data recorded in Table 3. HDAC8 shows no significant incorporation of Fe^{3+} or Ni^{2+} under the conditions tested. As initially prepared aerobically, the recombinant enzyme expressed in the presence of 100 μM $ZnCl_2$ contains predominantly Zn^{2+}, confirming that Zn^{2+} is bound in the active sites of HDAC8 structures published to date (*23*, *24*, *36*, *47*).

Of the transition metals that activate HDAC8, Fe^{2+} and Zn^{2+} exist in high amounts in the cell, with total concentrations around 0.1−0.2 mM in eukaryotes and *Escherichia coli* (*48*−*50*). Thus, these metal ions are the most likely native cofactors. The affinity of HDAC8 for Zn^{2+} and Fe^{2+} was measured from the metal-dependent activation of catalytic activity with the free metal concentration maintained using a metal buffer (Figure 2).

HDAC8 has significantly higher affinity for Zn^{2+} (K_D = 9 ± 1 pM) than Fe^{2+} (K_D = 1.1 ± 0.3 μM), consistent with the higher Lewis acidity of Zn^{2+} (*51*, *52*). At first glance, this disparity suggests that HDAC8 should be a Zn^{2+}-dependent enzyme. However, previous measurements in living cells indicate that the readily exchangeable concentration of Zn^{2+} ($[Zn^{2+}]_{free} \sim 10-400$ pM (*53*, *54*)) is also orders of magnitude lower than the readily exchangeable concentration of Fe^{2+} ($[Fe^{2+}_{free}] \sim 0.2-6$ μM) (*55*−*57*). The similarities between the metal affinities of HDAC8 and the readily exchangeable metal concentrations in cells suggest that HDAC8 is thermodynamically poised to be activated by either or both Zn^{2+} and Fe^{2+} *in vivo*. The metal content of HDAC8 affects both the catalytic activity and the inhibitor affinity *in vitro* (*27*). Therefore, altering the metal cofactor *in vivo* will affect the catalytic efficiency and, possibly, the affinity and selectivity toward acetylated substrates.

Table 4: Metal Ion Dependence of HDAC8 Inhibition

Inhibitor	K_i (nM)		
	Co^{2+}	Fe^{2+}	Zn^{2+}
M344 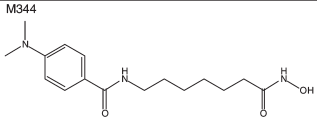	14.8 ± 0.8	63 ± 2	68 ± 6
SAHA[a] 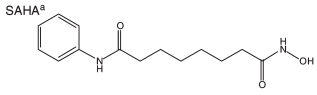	44 ± 15	130 ± 40	250 ± 25

[a]Reference *27*.

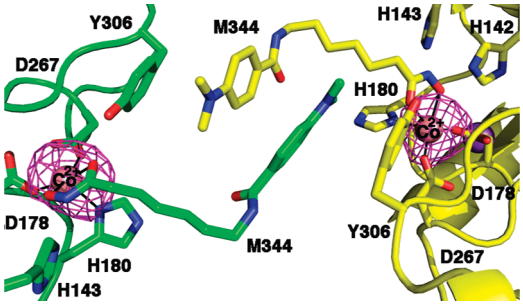

FIGURE 3: Bijvoet difference Fourier map of the wild-type human Co^{2+}-HDAC8-M344 complex calculated with X-ray diffraction data collected near the cobalt edge (7.725 keV) demonstrating the binding of Co^{2+} (contoured at 3σ). The enzyme packs as a crystallographic dimer with two molecules in the asymmetric unit; selected active site residues are indicated.

Finally, inhibition of HDAC8 by M344 was tested. The inhibition constant (K_i) is metal ion-dependent, and inhibition data are reported in Table 4. The inhibitory potency of M344 against metal-substituted HDAC8 enzymes is greatest with Co^{2+}-HDAC8 as compared to Fe^{2+}-HDAC8 and Zn^{2+}-HDAC8. A comparable metal-dependent affinity trend was previously reported for the inhibitor SAHA (*27*). This is consistent with the same functional group used by SAHA for metal coordination, a hydroxamate that forms a five-membered ring chelate complex.

Crystal Structures. To confirm metal binding in the crystal structures, X-ray diffraction data for wild-type and D101L HDAC8 enzymes were collected at incident wavelengths near the absorption edges of cobalt or iron. A strong peak in the Bijvoet difference Fourier map of the active site in each structure corresponds to a metal ion coordinated by D178, H180, and D267 (Figures 3 and 4). Considering that the absorption edges of cobalt or iron (7.7089 or 7.1120 keV, respectively) and the copper Kα (8.048 keV) are significantly lower than the absorption edge of zinc (9.6586 keV), the Bijvoet difference Fourier peaks confirm the binding of Co^{2+}, Fe^{2+}, or Mn^{2+} (Figure 4). These crystallographic results are consistent with the metal ion content of these protein samples determined in solution (Table 3). Refined metal ion coordination geometries and distances in the Co^{2+}-, Fe^{2+}-, and Mn^{2+}-substituted enzymes are comparable to those observed in Zn^{2+}-HDAC8 (Table 5).

Strong peaks in the Bijvoet difference Fourier maps are also observed at the sites corresponding to two previously reported monovalent cation binding sites (Figure 5) (*21*, *23*, *24*). Metal coordination distances average ~2.8−2.9 Å and are consistent with the binding of K^+ ions (absorption edge = 3.6074 eV), as previously reported (*24*).

In the structure of D101L Zn^{2+}-HDAC8 (*36*), a crystallographic dimer forms such that inhibitor binding in one monomer

Table 5: Average Metal Ion Coordination Distances (Å) in D101L HDAC8

catalytic metal ion	D178	D267	H180	W1[b]	W2[b]	hydroxamate (N−O, C═O)
Co^{2+}	2.0	2.0	2.1	2.8	2.1	1.8, 2.4
Fe^{2+}	1.9	2.0	2.1	2.1	2.2	1.9, 2.6
Mn^{2+}	2.1	2.0	2.2	2.0	2.3	2.2, 2.4
Zn^{2+}[a]	2.0	2.0	2.1	2.3	2.1	2.5, 2.3

[a]Reference *36*. [b]W1 is the water molecule that is closest to the binding site of the hydroxamate OH group, and W2 is the water molecule that is closest to the binding site of the hydroxamate C═O group.

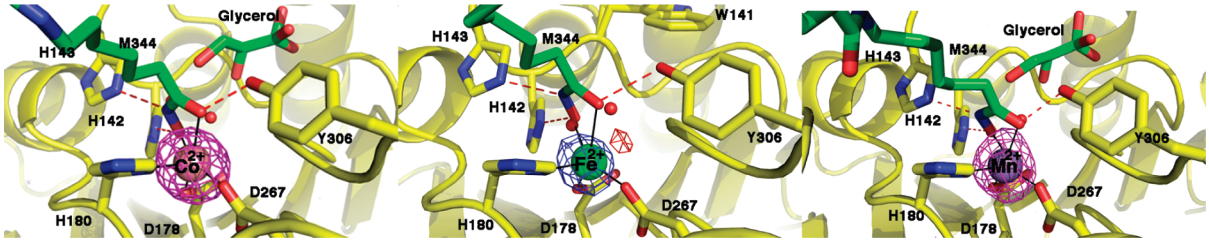

FIGURE 4: Bijvoet difference Fourier maps of the D101L Co^{2+}-, Fe^{2+}-, and Mn^{2+}-HDAC8-M344 complexes (left to right, respectively), calculated with X-ray diffraction data collected at the cobalt edge (7.725 keV), iron edge (7.120 keV), and the copper Kα (8.048 keV) demonstrating the binding of Co^{2+}, Fe^{2+}, and Mn^{2+}, respectively (contoured at 9σ, 4σ, and 4σ, respectively). Anomalous data collected using copper Kα radiation can include signal from Co^{2+}, Fe^{2+}, or Mn^{2+}, but excludes Zn^{2+}. In the Fe^{2+}-substituted enzyme, uninterpretable difference density is evident (red peak, contoured at 3σ) and may reflect incomplete changes in the metal coordination polyhedron. Protein atoms are color-coded as follows: carbon (protein, yellow; ligands, green), oxygen (red), and nitrogen (blue). Water molecules are represented as red spheres.

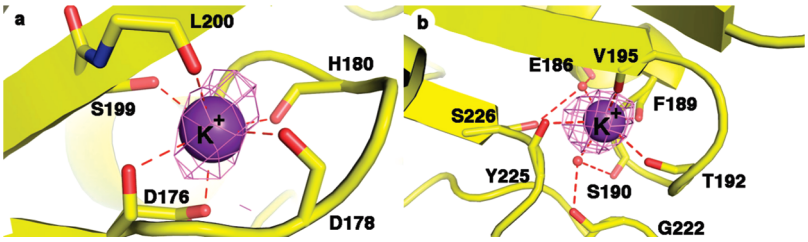

FIGURE 5: Bijvoet difference Fourier maps (contoured at 3σ) of K^+ ions bound in the two monovalent cation binding sites in the D101L Fe^{2+}-HDAC8-M344 complex. (a) Monovalent cation binding site adjacent to the active site. Metal ligands are color-coded as follows: carbon (yellow), oxygen (red), and nitrogen (blue). (b) Distal monovalent cation binding site. Atoms are color-coded as in (a), and water molecules are represented as red spheres.

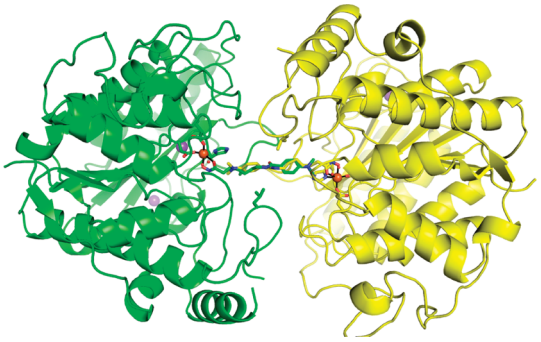

FIGURE 6: The crystallographic dimer of the D101L Fe^{2+}-HDAC8-M344 complex. Monomer A and monomer B are shown in green and yellow, respectively. Fe^{2+}-coordinating residues and L101 are shown as sticks. Protein atoms are color-coded as follows: carbon (green or yellow), oxygen (red), and nitrogen (blue). Ions are colored as follows: Fe^{2+} (orange) and K^+ (purple). Inhibitor M344 atoms are colored as follows: carbon (green or yellow), nitrogen (blue), and oxygen (red).

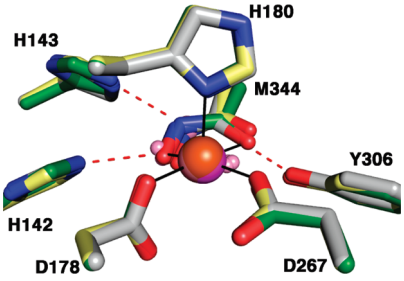

FIGURE 7: Square-pyramidal Co^{2+}, Fe^{2+}, and Mn^{2+} coordination polyhedra in the liganded and unliganded forms of D101L HDAC8 complexed with M344. Atoms are color-coded as follows: carbon = yellow for Fe^{2+} structure, gray for Co^{2+} structure, and green for Mn^{2+} structure, nitrogen = blue, oxygen = red, Fe^{2+} = orange sphere, Co^{2+} = pink sphere, Mn^{2+} = magenta sphere, and H_2O = small pink spheres. Metal coordination and hydrogen bond interactions involving the inhibitor hydroxamate group are shown in solid black and dotted red lines, respectively.

precludes inhibitor binding in the symmetry-related molecule (Figure 6), resulting in 50% inhibitor occupancy in each active site. Accordingly, there is also electron density consistent with 50% occupancy of two zinc-bound solvent molecules. Similar inhibitor binding and metal coordination interactions are observed in the structures of D101L Co^{2+}- or Fe^{2+}-HDAC8 (Figure 7), indicating that Zn^{2+}, Co^{2+}, and Fe^{2+} are each pentacoordinate with square-pyramidal geometry in the unliganded form of the enzyme. Smeared electron density is observed for the catalytic water molecule (W1) in the D101L Co^{2+}-HDAC8 complex (data not shown), which is satisfactorily fit with a single solvent molecule that refines to a position 2.8 Å away from the Co^{2+} ion with 25% occupancy. In the Fe^{2+}-substituted enzyme, a small 3.5σ electron density peak is seen ~1.5 Å from the Fe^{2+} center and is located close (~1.9 Å) to the metal-bound solvent molecules (Figure 4). This peak does not refine satisfactorily as a water molecule with full or partial occupancy, so we have not built anything into this density in the final model. Interestingly, D101L Mn^{2+}-HDAC8 crystallizes in space group $P2_12_12_1$ with two molecules in the asymmetric unit. The crystallographic symmetry formerly observed in the D101L Zn^{2+}-, Co^{2+}-, and Fe^{2+}-HDAC8 structures is broken due to unequal inhibitor occupancy in the two D101L Mn^{2+}-HDAC8 monomers in the asymmetric unit (30% in monomer A and 70% in monomer B). Electron density for two metal-bound solvent molecules is clearly visible only in monomer A with occupancy = 0.7. Both D101L Co^{2+}- and Mn^{2+}-HDAC8 reveal electron density adjacent to the active site which is best fit with a disordered glycerol molecule, as previously observed in D101L Zn^{2+}-HDAC8 (*36*). D101L Fe^{2+}-HDAC8 reveals electron density for two alternate conformations of W141.

DISCUSSION

Hydrolytic metalloenzymes can exhibit a wide range of catalytic activities when substituted with different transition metal ions. Here, it is instructive to compare metal ion−activity relationships in three enzymes that share the α/β arginase fold: arginase, HDAC8, and acetylpolyamine amidohydrolase (APAH). Carvajal and colleagues demonstrate that maximal human arginase I activity results from the binding of two Mn^{2+} ions, and the enzyme exhibits minimal activity levels with Ni^{2+} and Co^{2+}; the K_M value does not significantly change with different metal ions (*58*) (in contrast, Stone and colleagues report that Co^{2+}-substituted human arginase I exhibits significantly higher catalytic activity (*59*)). The APAH from *Mycoplana ramosa* exhibits a similar preference for Mn^{2+}, with the general metal ion−activity trend Mn^{2+} > Co^{2+} > Zn^{2+} > Mg^{2+} > Cu^{2+} > Ca^{2+}, but individual kinetic constants are not reported (*60*). In contrast, the HDAC enzymes were initially thought to be zinc metallohydrolases based on studies of the histone deacetylase-like protein from *A. aeolicus* (*21*), but HDAC8 exhibits the metal ion−activity dependence Co^{2+} > Fe^{2+} > Zn^{2+} > Ni^{2+} > Mn^{2+} based on k_{cat}/K_M values (*27*). While the k_{cat} value measured for HDAC8 is less sensitive to the identity of the divalent metal ion, the K_M values for Co^{2+}-HDAC8 and Fe^{2+}-HDAC8 are 160 and 210 μM, respectively, in comparison with that of 1100 μM measured for Zn^{2+}-HDAC8 (*27*); the low values of k_{cat}/K_M combined with the high value of K_M for the coumarin-labeled peptide substrates suggest that K_M likely reflects the substrate dissociation constant. Consistent with this, the enhanced activity of HDAC8 with fluorinated acetyl-L-lysine substrates suggests that deacetylation

is the rate-limiting step for k_{cat} (*61*, *62*). Additionally, the K_i values measured for the hydroxamate inhibitors SAHA (Vorinostat) and M344 indicate the preference $Co^{2+} > Fe^{2+} \approx Zn^{2+}$ (Table 4) (*27*). These data implicate a substrate−metal ion coordination interaction in the precatalytic Michaelis complex; moreover, as first noted by Fierke and colleagues, these data suggest that HDAC8 may be a Fe^{2+}-metalloenzyme *in vivo*, given the greater biological abundance of this metal ion (*27*).

However, the affinity of HDAC8 for Zn^{2+} is ~10^6-fold higher than Fe^{2+} affinity (Figure 2), which combined with the oxidation of Fe^{2+} to Fe^{3+} explains the purification of HDAC8 with bound zinc. A preference for Zn^{2+} binding is predicted by the increased Lewis acidity of Zn^{2+} compared to Fe^{2+} and is also in accord with the Irving−Williams series of stability constants (*51*, *52*). Nonetheless, it remains a possibility that HDAC8 binds either Fe^{2+} or Zn^{2+} *in vivo* since the current data indicate that intracellular concentrations of readily exchangeable Zn^{2+} are several orders of magnitude lower than readily exchangeable Fe^{2+} (5−400 pM vs 0.2−6 μM) (*53*−*57*). Assuming that metal selectivity is determined mainly based on thermodynamics, a competitive binding equation (eq 2) can be used to predict the fractional bound Zn^{2+} and Fe^{2+} at a given concentration of free Zn^{2+} and Fe^{2+}. These calculations demonstrate that in the expected physiological range of metal ion concentrations (10−400 pM $[Zn]_{free}$, 0.2−0.6 μM $[Fe]_{free}$), HDAC8 could either bind mainly Zn^{2+} (97% Zn/0.4% Fe) or Fe^{2+} (8% Zn/77% Fe), depending on the ratio of exchangeable Fe^{2+}/Zn^{2+} in the cell. Therefore, HDAC8 could be activated by either or both metal ions *in vivo*, and possibly, metal ion composition could vary depending on cellular conditions. However, the determinants of Fe^{2+}/Zn^{2+} metal selectivity in eukaryotic cells are currently unclear and could be facilitated by metallochaperones, or kinetic control, rather than thermodynamics (*63*). To date, no zinc-specific metallochaperones have been identified, although several potential iron-specific metallochaperones are being investigated for roles in iron homeostasis, particularly in the assembly of Fe-S clusters (*63*−*65*). Therefore, direct measurement of metal-bound HDAC8 *in vivo* will be required to definitively identify the native cofactor and to determine whether the metal content is variable.

$$\frac{E\cdot Fe}{E_{tot}} = \frac{1}{1+\frac{K_{Fe}}{[Fe]_{free}}\left(1+\frac{[Zn]_{free}}{K_{Zn}}\right)} \quad (2)$$

Intracellular metal ion homeostasis can be important for regulating metal binding to metalloenzymes. The eukaryotic Mn-dependent superoxide dismutase (SOD2) specifically acquires Mn in *Saccharomyces cerevisiae* but is inactive when Fe is bound. Deletion of a specific transporter, Mtm1p, results in elevated mitochondrial iron concentrations and an inactive Fe-SOD2 *in vivo* (*66*). It is also likely that metal ion binding to other metalloenzymes, such as HDAC8, is sensitive to intracellular homeostasis (reviewed in ref *63*).

Metal ions in metalloenzymes can affect enzyme function by maintaining the structure of the active site and providing coordination interactions for substrate, transition state(s), and intermediate(s) that facilitate catalysis. In the active site of arginase, Mn_A^{2+} is bound with square-pyramidal geometry by four protein ligands (Asp_3His), and Mn_B^{2+} is bound with octahedral geometry by four protein ligands (Asp_3His); one aspartate, D234, serves as a bidentate ligand (*20*). Two aspartates and one hydroxide ion serve as bridging ligands. The Mn_B^{2+} site of arginase corresponds to the single metal binding site of HDAC enzymes (*67*, *68*). In HDAC8 substituted with Zn^{2+}, Co^{2+}, and Fe^{2+}, the divalent metal ion is coordinated by three protein ligands (Asp_2His) and two water molecules with square-pyramidal geometry. Inspection of the HDAC8 active site suggests that D267, which corresponds to D234 of arginase, cannot achieve a bidentate coordination geometry to yield an octahedral coordination polyhedron. Interestingly, one of the monovalent cation binding sites in HDAC8 includes the backbone C=O groups of two of the three divalent metal ion coordination residues (H180 and D178) (Figure 5), and potassium binding to this site inhibits catalytic activity (*69*). It appears that HDAC8 has evolved to favor square-pyramidal metal coordination where the substrate C=O group displaces one of the metal-bound water molecules and coordinates to an equatorial site in the precatalytic Michaelis complex. No significant changes are observed between the crystal structures of wild-type Zn^{2+}- and Co^{2+}-HDAC8 (rms deviation = 0.40 Å for 331 Cα atoms) or D101L Co^{2+}, Fe^{2+}, Mn^{2+}, and Zn^{2+}-HDAC8 bound with M344 (approximate rms deviations = 0.15 Å for 335 Cα atoms). The visible absorption spectra of Co^{2+}-HDAC8 with and without inhibitor trichostatin A reveal no significant differences, consistent with similar Co^{2+} coordination geometries between the unliganded and liganded states (*70*). It is notable that square-pyramidal metal coordination geometry is also shared by the bacterial deacetylase UDP-3-*O*-((*R*)-3-hydroxymyristoyl)-*N*-acetylglucosamine deacetylase (LpxC), which has an $AspHis_2$ ligand set for Zn^{2+} coordination and an $\alpha+\beta$ fold unrelated to the α/β fold of HDAC8 (*71*, *72*).

In contrast to substrate binding in HDAC8, the guanidinium group of L-arginine does not coordinate to the metal ions in the precatalytic enzyme−substrate complex with $Mn^{2+}{}_2$-arginase, as indicated by the lack of metal dependence of K_M values (which reflect substrate binding affinity) (*58*, *73*). The K_M value is similarly invariant upon mutation of Mn^{2+} ligands, which alters metal ion occupancy and stoichiometry in the binuclear manganese cluster (*74*). Stability constants for metal ion chelation by ethylenediamine ligands are ranked $Mn^{2+} < Fe^{2+} < Co^{2+}$, $Zn^{2+} < Ni^{2+}$, consistent with less favorable guanidino−Mn^{2+} interactions (*75*). It would seem that in a system where a precatalytic substrate−metal coordination interaction is not important, the metal ion with the smaller stability constant is favored. In contrast, in the HDAC enzymes where a precatalytic C=O···metal coordination interaction is important, metal ions with larger stability constants are favored (for reference, acetylacetone binding constants rank in the order $Mn^{2+} < Zn^{2+} < Co^{2+}$; Fe^{2+} data not currently available (*75*)). Moreover, the substitution of one metal ion for another could alter the mechanism of catalysis with regard to precatalytic substrate−metal interactions. For example, a decrease in K_M has recently been observed for $Co^{2+}{}_2$-human arginase I, suggesting that metals with greater stability constants could favor guanidino−metal coordination in the precatalytic enzyme−substrate complex (*59*). In the bacterial deacetylase LpxC, metal substitution affects the value of k_{cat} rather than K_M with a metal reactivity trend that is similar to HDAC8 ($Mn^{2+} < Zn^{2+} < Fe^{2+} < Co^{2+}$) (*35*, *76*). In this case, it is possible that the C=O···metal coordination interaction occurs in the transition state rather than the ground state. Given that LpxC and HDAC8 adopt unrelated protein folds, it is reasonable to expect structure−function differences between these two metalloamidases.

In conclusion, the ability of divalent metal ions to adopt specific geometries generally is vital for proper enzyme function,

and enzymes utilize specific ligand sets to select for desired metal cofactors. The ligand set of HDAC8 (Asp_2His) is unusual for Zn^{2+} binding within the greater family of zinc enzymes (*77*, *78*). While HDAC enzymes are thought to be Zn^{2+}-hydrolases, it is intriguing that greater catalytic efficiencies result with Co^{2+} or Fe^{2+} substitution in HDAC8 (*27*). Here, metal reconstitution experiments in solution and in the crystal confirm stoichiometric binding of these divalent metal ions and reveal conservation of square-pyramidal metal coordination geometry regardless of the specific metal ion bound. Metal affinity measurements show that HDAC8 binds Zn^{2+} approximately 10^6-fold more tightly than Fe^{2+}; however, since concentrations of readily exchangeable Zn^{2+} are considerably lower than Fe^{2+} (5−400 pM vs 0.2−6 μM) (*53*−*57*), HDAC8 may be activated *in vivo* by either or both of these metals depending on cellular concentrations. Because metallochaperones may influence metal trafficking *in vivo*, further analysis of endogenous HDAC8 is warranted to confirm metal ion preference *in vivo*.

ACKNOWLEDGMENT

This work is based upon research conducted at the Northeastern Collaborative Access Team beamlines of the Advanced Photon Source, which is supported by Award RR-15301 from the National Center for Research Resources at the National Institutes of Health, and beamline X25 of the National Synchrotron Light Source, which is supported principally from the Offices of Biological and Environmental Research and of Basic Energy Sciences of the U.S. Department of Energy and from the National Center for Research Resources of the National Institutes of Health.

REFERENCES

1. Walsh, C. T. (2006) Posttranslational modification of proteins: expanding nature's inventory, Roberts and Co., Englewood, CO.
2. Kouzarides, T. (2007) Chromatin modifications and their function. *Cell 128*, 693–705.
3. Seo, J., and Lee, K. J. (2004) Post-translational modifications and their biological functions: proteomic analysis and systematic approaches. *J. Biochem. Mol. Biol. 37*, 35–44.
4. Santos-Rosa, H., and Caldas, C. (2005) Chromatin modifier enzymes, the histone code and cancer. *Eur. J. Cancer 41*, 2381–2402.
5. Lennartsson, A., and Ekwall, K. (2009) Histone modification patterns and epigenetic codes. *Biochim. Biophys. Acta 1790*, 863–868.
6. Choi, J. K., and Howe, L. J. (2009) Histone acetylation: truth of consequences? *Biochem. Cell Biol. 87*, 139–150.
7. Luger, K., Mäder, A. W., Richmond, R. K., Sargent, D. F., and Richmond, T. J. (1997) Crystal structure of the nucleosome core particle at 2.8 Å resolution. *Nature 389*, 251–260.
8. Mujtaba, S., Zeng, L., and Zhou, M.-M. (2007) Structure and acetyl-lysine recognition of the bromodomain. *Oncogene 26*, 5521–5527.
9. Dhalluin, C., Carlson, J. E., Zeng, L., He, C., Aggarwal, A. K., Zhou, M.-M., and Zhou, M.-M. (1999) Structure and ligand of a histone acetyltransferase bromodomain. *Nature 399*, 491–496.
10. Sanchez, R., and Zhou, M.-M. (2009) The role of human bromodomains in chromatin biology and gene transcription. *Curr. Opin. Drug Discovery Dev. 12*, 659–665.
11. Chan, D. W., Wang, Y., Wu, M., Wong, J., Qin, J., and Zhao, Y. (2009) Unbiased proteomic screen for binding proteins to modified lysines on histone H3. *Proteomics 9*, 2343–2354.
12. Li, S., and Shogren-Knaak, M. A. (2008) The Gcn5 bromodomain of the SAGA complex facilitates cooperative and cross-tail acetylation of nucleosomes. *J. Biol. Chem. 284*, 9411–9417.
13. Gregoretti, I. V., Lee, Y.-M., and Goodson, H. V. (2004) Molecular evolution of the histone deacetylase family: functional implications of phylogenetic analysis. *J. Mol. Biol. 338*, 17–31.
14. Taunton, J., Hassig, C. A., and Schreiber, S. L. (1996) A mammalian histone deacetylase related to the yeast transcriptional regulator Rpd3p. *Science 272*, 408–411.
15. Lin, H.-Y., Chen, C.-S., Lin, S.-P., Weng, J.-R., and Chen, C.-S. (2006) Targeting histone deacetylase in cancer therapy. *Med. Res. Rev. 26*, 397–413.
16. Yang, W.-M., Tsai, S.-C., Wen, Y.-D., Fejér, G., and Seto, E. (2002) Functional domains of histone deacetylase-3. *J. Biol. Chem. 277*, 9447–9454.
17. Hu, E., Chen, Z., Fredrickson, T., Zhu, Y., Kirkpatrick, R., Zhang, G.-F., Johanson, K., Sung, C.-M., Liu, R., and Winkler, J. (2000) Cloning and characterization of a novel human class I histone deacetylase that functions as a transcription repressor. *J. Biol. Chem. 275*, 15254–15264.
18. Waltregny, D., de Leval, L., Glénisson, W., Ly Tran, S., North, B. J., Bellahcène, A., Weidle, U., Verdin, E., and Castronovo, V. (2004) Expression of histone deacetylase 8, a class I histone deacetylase, is restricted to cells showing smooth muscle differentiation in normal human tissues. *Am. J. Pathol. 165*, 553–564.
19. Martin, M., Kettmann, R., and Dequiedt, F. (2007) Class IIa histone deacetylases: regulating the regulators. *Oncogene 26*, 5450–5467.
20. Kanyo, Z. F., Scolnick, L. R., Ash, D. E., and Christianson, D. W. (1996) Structure of a unique binuclear manganese cluster in arginase. *Nature 383*, 554–557.
21. Finnin, M. S., Donigian, J. R., Cohen, A., Richon, V. M., Rifkind, R. A., Marks, P. A., Breslow, R., and Pavletich, N. P. (1999) Structures of a histone deacetylase homologue bound to the TSA and SAHA inhibitors. *Nature 401*, 188–193.
22. Nielsen, T. K., Hildmann, C., Dickmanns, A., Schwienhorst, A., and Ficner, R. (2005) Crystal structure of a bacterial class 2 histone deacetylase homologue. *J. Mol. Biol. 354*, 107–120.
23. Somoza, J. R., Skene, R. J., Katz, B. A., Mol, C., Ho, J. D., Jennings, A. J., Luong, C., Arvai, A., Buggy, J. J., Chi, E., Tang, J., Sang, B.-C., Verner, E., Wynands, R., Leahy, E. M., Dougan, D. R., Snell, G., Navre, M., Knuth, M. W., Swanson, R. V., McRee, D. E., and Tari, L. W. (2004) Structural snapshots of human HDAC8 provide insights into the class I histone deacetylases. *Structure 12*, 1325–1334.
24. Vannini, A., Volpari, C., Filocamo, G., Casavola, E. C., Brunetti, M., Renzoni, D., Chakravarty, P., Paolini, C., De Francesco, R., Gallinari, P., Steinkühler, C., and Di Marco, S. (2004) Crystal structure of a eukaryotic zinc-dependent histone deacetylase, human HDAC8, complexed with a hydroxamic acid inhibitor. *Proc. Natl. Acad. Sci. U.S.A. 101*, 15064–15069.
25. Bottomley, M. J., Lo Surdo, P., Di Giovine, P., Cirillo, A., Scarpelli, R., Ferrigno, F., Jones, P., Neddermann, P., De Francesco, R., Steinkühler, C., Gallinari, P., and Carfi, A. (2008) Structural and functional analysis of the human HDAC4 catalytic domain reveals a regulatory structural zinc-binding domain. *J. Biol. Chem. 283*, 26694–26704.
26. Schuetz, A., Min, J., Allali-Hassani, A., Schapira, M., Shuen, M., Loppnau, P., Mazitschek, R., Kwiatkowski, N. P., Lewis, T. A., Maglathin, R. L., McLean, T. H., Bochkarev, A., Plotnikov, A. N., Vedadi, M., and Arrowsmith, C. H. (2008) Human HDAC7 harbors a class IIa histone deacetylase-specific zinc binding motif and cryptic deacetylase activity. *J. Biol. Chem. 283*, 11355–11363.
27. Gantt, S. L., Gattis, S. G., and Fierke, C. A. (2006) Catalytic activity and inhibition of human histone deacetylase 8 is dependent on the identity of the active site metal ion. *Biochemistry 45*, 6170–6178.
28. Tripp, B. C., Bell, C. B., III, Cruz, F., Krebs, C., and Ferry, J. G. (2004) A role for iron in an ancient carbonic anhydrase. *J. Biol. Chem. 279*, 6683–6687.
29. Seffernick, J. L., McTavish, H., Osborne, J. P., de Souza, M. L., Sadowsky, M. J., and Wackett, L. P. (2002) Atrazine chlorohydrolase from *Pseudomonas* sp. strain ADP is a metalloenzyme. *Biochemistry 41*, 14430–14437.
30. Zhu, J., Dizin, E., Hu, X., Wavreille, A.-S., Park, J., and Pei, D. (2003) S-Ribosylhomocysteinase (LuxS) is a mononuclear iron protein. *Biochemistry 42*, 4717–4726.
31. D'souza, V. M., and Holz, R. C. (1999) The methionyl aminopeptidase from *Escherichia coli* can function as an iron(II) enzyme. *Biochemistry 38*, 11079–11085.
32. Rajagopalan, P. T. R., Grimme, S., and Pei, D. (2000) Characterization of cobalt(II)-substituted peptide deformylase: function of the metal ion and the catalytic residue glu-133. *Biochemistry 39*, 779–790.
33. Copik, A. J., Waterson, S., Swierczek, S. I., Bennett, B., and Holz, R. C. (2005) Both nucleophile and substrate bind to the catalytic Fe(II)-center in the type-II methionyl aminopeptidase from *Pyrococcus furiousus*. *Inorg. Chem. 44*, 1160–1162.
34. Porter, D. J. T., and Austin, E. A. (1993) Cytosine deaminase. The roles of divalent metal ions in catalysis. *J. Biol. Chem. 268*, 24005–24011.
35. Hernick, M., Gattis, S. G., Penner-Hahn, J. E., and Fierke, C. A. (2010) Activation of *Escherichia coli* UDP-3-O-[(R)-3-hydroxymyristoyl]-N-acetylglucosamine deacetylase by Fe^{2+} yields a more

efficient enzyme with altered ligand affinity. *Biochemistry 49*, 2246–2255.
36. Dowling, D. P., Gantt, S. L., Gattis, S. G., Fierke, C. A., and Christianson, D. W. (2008) Structural studies of human histone deacetylase 8 and its site-specific variants complexed with substrate and inhibitors. *Biochemistry 47*, 13554–13563.
37. Bradford, M. M. (1976) A rapid and sensitive method for the quantitation of microgram quantities of protein utilizing the principle of protein-dye binding. *Anal. Biochem. 72*, 248–254.
38. Cheng, Y., and Prusoff, W. H. (1973) Relationship between the inhibition constant (K_I) and the concentration of inhibitor which causes 50% inhibition (I_{50}) of an enzymatic reaction. *Biochem. Pharmacol. 22*, 3099–3108.
39. Jung, M., Brosch, G., Kölle, D., Scherf, H., Gerhäuser, C., and Loidl, P. (1999) Amide analogues of trichostatin A as inhibitors of histone deacetylase and inducers of terminal cell differentiation. *J. Med. Chem. 42*, 4669–4679.
40. Otwinowski, Z., and Minor, W. (1997) Processing of X-ray diffraction data collected in oscillation mode. *Methods Enzymol. 276*, 307–326.
41. McCoy, A. J., Grosse-Kunstleve, R. W., Adams, P. D., Winn, M. D., Storoni, L. C., and Read, R. J. (2007) Phaser crystallographic software. *J. Appl. Crystallogr. 40*, 658–674.
42. Brünger, A. T., Adams, P. D., Clore, G. M., Delano, W. L., Gros, P., Grosse-Kunstleve, R. W., Jiang, J.-S., Kuszewski, J., Nilges, M., Pannu, N. S., Read, R. J., Rice, L. M., Simonson, T., and Warren, G. L. (1998) Crystallography & NMR system: a new software suite for macromolecular structure determination. *Acta Crystallogr. D 54*, 905–921.
43. Murshudov, G. N., Vagin, A. A., and Dodson, E. J. (1997) Refinement of macromolecular structures by the maximum-likelihood method. *Acta Crystallogr. D 53*, 240–255.
44. Emsley, P., and Cowtan, K. (2004) Coot: model-building tools for molecular graphics. *Acta Crystallogr. D 60*, 2126–2132.
45. McCall, K. A., and Fierke, C. A. (2004) Probing determinants of the metal ion selectivity in carbonic anhydrase using mutagenesis. *Biochemistry 43*, 3979–3986.
46. McCall, K. A., and Fierke, C. A. (2000) Colorimetric and fluorimetric assays to quantitate micromolar concentrations of transition metals. *Anal. Biochem. 284*, 307–315.
47. Vannini, A., Volpari, C., Gallinari, P., Jones, P., Mattu, M., Carfi, A., De Francesco, R., Steinkühler, C., and Di Marco, S. (2007) Substrate binding to histone deacetylases as shown by the crystal structure of the HDAC8-substrate complex. *EMBO Rep. 8*, 879–884.
48. Espósito, B. P., Epsztejn, S., Breuer, W., and Cabantchik, Z. I. (2002) A review of fluorescence methods for assessing labile iron in cells and biological fluids. *Anal. Biochem. 304*, 1–18.
49. Outten, C. E., and O'Halloran, T. V. (2001) Femtomolar sensitivity of metalloregulatory proteins controlling zinc homeostasis. *Science 292*, 2488–2492.
50. Vallee, B. L., and Falchuk, K. H. (1993) The biochemical basis of zinc physiology. *Physiol. Rev. 73*, 79–118.
51. Lippard, S. J., and Berg, J. M. (1994) Principles of bioinorganic chemistry, Vol. *XVII*, University Science Books, Mill Valley, CA.
52. Irving, J. T., and Williams, J. P. (1948) Order of stability of metal complexes. *Nature 162*, 746–747.
53. Bozym, R. A., Thompson, R. B., Stoddard, A. K., and Fierke, C. A. (2006) Measuring picomolar intracellular exchangeable zinc in PC-12 cells using a ratiometric fluorescence biosensor. *ACS Chem. Biol. 1*, 103–111.
54. Vinkenborg, J. L., Nicolson, T. J., Bellomo, E. A., Koay, M. S., Rutter, G. A., and Merkx, M. (2009) Genetically encoded FRET sensors to monitor intracellular Zn^{2+} homeostasis. *Nat. Methods 6*, 737–740.
55. Epsztejn, S., Kakhlon, O., Glickstein, H., Breuer, W., and Cabantchik, Z. I. (1997) Fluorescence analysis of the labile iron pool of mammalian cells. *Anal. Biochem. 248*, 31–40.
56. MacKenzie, E. L., Iwasaki, K., and Tsuji, Y. (2008) Intracellular iron transport and storage: from molecular mechanisms to health implications. *Antioxid. Redox Signaling 10*, 997–1030.
57. Petrat, F., de Groot, H., and Rauen, U. (2001) Subcellular distribution of chelatable iron: a laser scanning microscopic study in isolated hepatocytes and liver endothelial cells. *Biochem. J. 356*, 61–69.
58. Carvajal, N., Torres, C., Uribe, E., and Salas, M. (1995) Interaction of arginase with metal ions: studies of the enzyme from human liver and comparison with other arginases. *Comp. Biochem. Physiol., Part B: Biochem. Mol. Biol. 112*, 153–159.
59. Stone, E. M., Glazer, E. S., Chantranupong, L., Cherukuri, P., Breece, R. M., Tierney, D. L., Curley, S. A., Iverson, B. L., and Georgiou, G. (2010) Replacing Mn^{2+} with Co^{2+} in human arginase I enhances cytotoxicity toward L-arginine auxotrophic cancer cell lines. *ACS Chem. Biol. 5*, 333–342.
60. Sakurada, K., Ohta, T., Fujishiro, K., Hasegawa, M., and Aisaka, K. (1996) Acetylpolyamine amidohydrolase from *Mycoplana ramosa*: gene cloning and characterization of the metal-substituted enzyme. *J. Bacteriol. 178*, 5781–5786.
61. Riester, D., Wegener, D., Hildmann, C., and Schwienhorst, A. (2004) Members of the histone deacetylase superfamily differ in substrate specificity towards small synthetic substrates. *Biochem. Biophys. Res. Commun. 324*, 1116–1123.
62. Smith, B. C., and Denu, J. M. (2007) Acetyl-lysine analog peptides as mechanistic probes of protein deacetylases. *J. Biol. Chem. 282*, 37256–37265.
63. Waldron, K. J., Rutherford, J. C., Ford, D., and Robinson, N. J. (2009) Metalloproteins and metal sensing. *Nature 460*, 823–830.
64. Mansy, S. S., and Cowan, J. A. (2004) Iron-sulfur cluster biosynthesis: toward an understanding of cellular machinery and molecular mechanism. *Acc. Chem. Res. 37*, 719–725.
65. Tottey, S., Harvie, D. R., and Robinson, N. J. (2005) Understanding how cells allocate metals using metal sensors and metallochaperones. *Acc. Chem. Res. 38*, 775–783.
66. Yang, M., Cobine, P. A., Molik, S., Naranuntarat, A., Lill, R., Winge, D. R., and Culotta, V. C. (2006) The effects of mitochondrial iron homeostasis on cofactor specificity of superoxide dismutase 2. *EMBO J. 25*, 1775–1783.
67. Christianson, D. W. (2005) Arginase: structure, mechanism, and physiological role in male and female sexual arousal. *Acc. Chem. Res. 38*, 191–201.
68. Dowling, D. P., Di Costanzo, L., Gennadios, H. A., and Christianson, D. W. (2008) Evolution of the arginase fold and functional diversity. *Cell. Mol. Life Sci. 65*, 2039–2055.
69. Gantt, S. L., Joseph, C. G., and Fierke, C. A. (2009) Activation and inhibition of histone deacetylase 8 by monovalent cations. *J. Biol. Chem. 285*, 6036–6043.
70. Gantt, S. L. (2006) Ph.D. Dissertation, University of Michigan, Ann Arbor.
71. Mochalkin, I., Knafels, J. D., and Lightle, S. (2008) Crystal structure of LpxC from *Pseudomonas aeruginosa* complexed with the potent BB-78485 inhibitor. *Protein Sci. 17*, 450–457.
72. Whittington, D. A., Rusche, K. M., Shin, H., Fierke, C. A., and Christianson, D. W. (2003) Crystal structure of LpxC, a zinc-dependent deacetylase essential for endotoxin biosynthsis. *Proc. Natl. Acad. Sci. U.S.A. 100*, 8146–8150.
73. Carvajal, N., Uribe, E., and Torres, C. (1994) Subcellular localization, metal ion requirement and kinetic properties of arginase from the gill tissue of the bivalve *Semele solida*. *Comp. Biochem. Physiol 109B*, 683–689.
74. Cama, E., Emig, F. A., Ash, D. E., and Christianson, D. W. (2003) Structural and functional importance of first-shell metal ligands in the binuclear manganese cluster of arginase I. *Biochemistry 42*, 7748–7758.
75. Martell, A. E., and Smith, R. M. (1974−1989) Critical Stability Constants, Vol. *1*−*6*, Plenum Press, New York.
76. Jackman, J. E., Raetz, C. R. H., and Fierke, C. A. (1999) UDP-3-O-(R-3-hydroxymyristoyl)-N-acetylglucosamine deacetylase of *Escherichia coli* is a zinc metalloenzyme. *Biochemistry 38*, 1902–1911.
77. Lipscomb, W. N., and Sträter, N. (1996) Recent advances in zinc enzymology. *Chem. Rev. 96*, 2375–2434.
78. Hernick, M., and Fierke, C. A. (2005) Zinc hydrolases: the mechanisms of zinc-dependent deacetylases. *Arch. Biochem. Biophys. 433*, 71–84.